Determination of equivalent black carbon mass concentration from aerosol light absorption using variable mass absorption cross-section

Weilun Zhao[1], Wangshu Tan[1,2], Gang Zhao[1,3], Chuanyang Shen[1], Yingli Yu[4,1], Chunsheng Zhao[1]

[1]Department of Atmospheric and Oceanic Sciences, School of Physics, Peking University, Beijing 100871, China

[2]School of Optics and Photonics, Beijing Institute of Technology, Beijing 100081, China

[3]State Key Joint Laboratory of Environmental Simulation and Pollution Control, College of Environmental Sciences and Engineering, Peking University, Beijing 100871, China

[4]Economics & Technology Research Institute, China National Petroleum Corporation, Beijing 100724, China

Correspondence to: Chunsheng Zhao (zcs@pku.edu.cn)

Abstract. Atmospheric black carbon (BC) is the strongest solar radiative absorber in the atmosphere, exerting significant influences on the earth's radiation budget. The mass absorption cross-section (MAC) is a crucial parameter for converting light absorption coefficient (σ_{ab}) to equivalent BC mass concentration (EBC). Traditional filter-based instrument, such as AE33, uses a constant MAC of 7.77 m^2/g at 880 nm to derive EBC, which may lead to uncertainty in EBC. In this paper, a new method of converting σ_{ab} to EBC is proposed by incorporating the variations of MAC attributed to the influences of aerosol coating state. Mie simulation showed that MAC varied dramatically with different core sizes and shell thicknesses. We compared our new method with traditional method during a field measurement at a site of North China Plain. The results showed that the MAC at 880 nm was smaller (larger) than 7.77 m^2/g for particle smaller (larger) than 280 nm, resulting in EBC mass size distribution derived from new method was higher (lower) than traditional method for particle smaller (larger) than 280 nm. Size-integrated EBC derived from the new method was 16% higher than traditional method. Sensitivity analysis indicated that the uncertainty in EBC caused by refractive index (RI) was within 35% and the imaginary part of RI had dominant influence on the derived EBC. This study emphasizes the necessity to take variations of MAC into account when deriving EBC from σ_{ab} and can help constrain the uncertainty in EBC measurements.

1 Introduction

Black carbon (BC) is an important component of atmospheric aerosol particles. The warming effect of BC is only second to that of carbon dioxide (Ramanathan and Carmichael, 2008) because of its highly absorbing property. The environmental effect of BC is nonnegligible. The absorption of BC can significantly reduce visibility (Moosmuller et al., 2009). BC are considered a major factor of adverse health disease (Highwood and Kinnersley, 2006). The fractal aggregates morphology of BC provides substantial surface area for deposition of cancerogenic matter. The insoluble nature and fine size of BC make it deposit in the lung for a long time. Because the significant impact of BC, extensive measurement has been made to monitor atmospheric loading of BC and give reference to policymaker for mitigation.

The BC mass concentration (m_{BC}) is one of the important variables for BC measurement (Bond et al., 2013). Many methods have been proposed to determine m_{BC}. For instance, the single-particle soot photometer (SP2) measure refractory BC (rBC) based on laser-induced incandescence (Schwarz et al., 2006). The organic carbon/elemental carbon (OCEC) analyzer determines elemental

carbon (EC) through heating collected sample in a subsequent helium/oxygen environment (Wu et al., 2012). Soot particle aerosol mass spectrometry (SP-AMS) combines laser-induced incandescence as well as laser vaporization used in mass spectrometry (Onasch et al., 2012) and also reports m_{BC} as rBC. However, the abovementioned instruments are complicated in structure, highly expensive, hard to maintain, as a result, not widely used.

Filter-based instruments, such as aethalometer (Hansen et al., 1984), are commonly used for routine BC observations and dedicated campaigns (Castagna et al., 2019;Sandradewi et al., 2008;Helin et al., 2018) because they are convenient and easy to maintain. Aethalometer does not directly measure m_{BC} and actually measures light absorption. Aethalometer converts absorption coefficient (σ_{ab}) at 880 nm to equivalent BC mass concentration (EBC) (Petzold et al., 2013) through a fixed mass absorption cross-section (MAC, 7.77 m^2/g at 880 nm). However, field measurements indicated that MAC showed both large temporal and spatial variability (Bond and Bergstrom, 2006;Lack et al., 2012;Cappa et al., 2012). For example, Bond et al. (2006) reported MAC at 550 nm varying from 1.6 to 15.9 m^2/g. Sharma et al. (2002) reported MAC at 880 nm varying from 6.4 to 28.3 m^2/g. It is not appropriate to use a fixed MAC at when EBC is derived from σ_{ab} at 880 nm. The variation of MAC has to be taken into account to reduce the uncertainty in the σ_{ab}-derived EBC.

The mixing state of BC is one of the crucial reasons leading to large variation in MAC. Field measurements have indicated that fresh BC particles are generally subject to several coating processes while being transported in the atmosphere and tend to be covered in layers of other organic or inorganic components (Shiraiwa et al., 2007;Cappa et al., 2019;Bond et al., 2006). The gathered shell that builds up on the BC core, acting as a lens to focus additional incident light on the enclosed BC core, can enhance BC light absorption (Fuller et al., 1999). As a result, a coated BC particle will have a bigger MAC than the original pure BC particle. This light absorption enhancement is termed as "lensing effect" of the BC-containing particles. For typical core-coating mixed BC-containing particles, this lensing effect was found to enhance BC absorption by 50-100% (Bond et al., 2006). Schwarz et al. (2008) found that fresh soot particles internally mixed with sulfates and organics during transportation, and the lensing effect enhanced the light absorption by a factor of 1.3-1.5.

At a given wavelength, such as 880 nm, the value of MAC relies on the size and the location of BC core, coating thickness, as well as refractive index (RI) (Fuller et al., 1999;Lack and Cappa, 2010). A simplified core-shell configuration has been introduced to illustrate the structure of BC-containing particles and calculate the relevant optical properties. Several studies have demonstrated that it is appropriate to use the core-shell configuration for aged aerosol (Majdi et al., 2020;Liu et al., 2019;Li et al., 2019).

In the previous studies (Zhao et al., 2019b;Ran et al., 2016a;Ran et al., 2016b;Castagna et al., 2019), the variation of MAC due to mixing state was not considered when deriving EBC from σ_{ab}. With the objective of improving the reliability of σ_{ab}-derived EBC, the Mie model incorporated with core-shell configuration hypothesis was applied in this study to assess the limitation of fixed MAC on σ_{ab}-derived EBC. Based on the detailed analysis of the relationship among MAC, D_{BC}, and coating thickness (T_{shell}), a modified approach considering variation of MAC due to mixing state was proposed for filter-based instruments to derive EBC from σ_{ab}. Detailed uncertainty analysis is carried out to assess the influence of assumptions used in this study. This modified method estimates size-resolvoled EBC accurately and reduces the uncertainty in σ_{ab}-derived EBC with respect to mixing state.

2 Dataset and instrumentation

2.1 Measurement sites

The EBC particle mass size distribution (BCPMSD) was obtained at the Zhangqiu Meteorology Station (36°42'N, 117°30'E), Shandong Province, surrounded by farmland and residential areas and a typical site for regional background conditions of North China Plain (NCP). The field campaign lasted for about 1 month, from July 23, 2017 to August 24, 2017.

The number fraction of BC-containing aerosol (N_{BC}) is required during conversion from absorption to EBC. N_{BC} was not measured simultaneously at Zhangqiu due to limitation in instruments. N_{BC} is a reference value in this work and referred from measurement at Taizhou (32°35'N, 119°57'E). An SP2 was used to determine N_{BC} at Taizhou from May 24, 2018 to June 18, 2018. The suburban site Taizhou lies at the south end of Jianghuai Plain in the East of China. This industrial area between the two megacities of Nanjing and Shanghai has experienced severe pollution during the past thirty years. Hence, N_{BC} measured at Taizhou is representative and the campaign averaged N_{BC} is used in this work. Besides, comparison between AE33 and the three-wavelength photoacoustic soot spectrometer (PASS-3) at 405 nm, 532 nm and 781 nm (Zhao et al., 2020) was also carried out at Taizhou for scattering correction of AE33.

Besides Taizhou, the comparison between AE33 and PASS-3 was also conducted from March 20, 2018 to April 30, 2018 and from October 10, 2018 to October 19, 2018 in Peking University (39°59'N, 116°18'E). This site is located at the northwest of Beijing, a megacity experiencing severe and complex urban pollution. From March 21, 2017 to April 9, 2017 at the Peking University site, simultaneous measurements of aethalometer AE51 (model 51, microAeth, USA) and AE33 at 880 nm were carried out to investigate the consistency between AE51 and AE33.

2.2 Instruments

All the measurements in the three sites were conducted in temperature (24 ± 2 °C) controlled containers, and a particle pre-impactor was used to remove particles larger than 10 μm from the input air stream. The drying systems in the three sites were configured with a Nafion dryer to keep the relative humidity of sample flow below 40%. This type of dryer performs well in reducing aerosol losses. The transmission efficiency of the Nafion dryer is up to 90% for particles smaller than 10 nm and rises up to 100% for particles larger than 30 nm (The performance details of the Nafion dryer can be accessed at http://www.permapure.com).

During the field campaign at the Zhangqiu site, the particle number size distribution (PNSD) as well as BCPMSD were simultaneously determined using the measurement system developed by Ning et al. (2013) and improved by Zhao et al. (2019b). The polydisperse aerosol sample flow was first drawn into DMA (Model 3080, TSI, USA) to select relatively monodispersed aerosol sub-populations with diameters ranging from 97 to 602 nm. Sheath and sample flows were set as 3 and 0.5 L/min, respectively. The selected monodispersed aerosol populations were further divided into two paths. One path (0.2 L/min) was drawn into AE51 for EBC measurements. The other path (0.3 L/min) was analyzed using CPC (model 3772, TSI, USA) for number concentration measurements. As the standard sample flow for CPC 3772 is 1 L/min, a cleaned airflow of 0.7 L/min was added for compensation. A BCPMSD cycle measured here required 5 min and we averaged the data with a temporal resolution of 2 hours.

The dry aerosol scattering coefficients at 525 nm were measured simultaneously to represent air pollution condition by an integrated

nephelometer (Ecotech Pty Ltd., Aurora 3000) with flowrate of 3 L/min and temporal resolution of 1 min. Similar to the measured BCPMSD, aerosol scattering coefficients were also averaged with a temporal resolution of 2 hours.

For AE51, the influence of loading effect was resolved by using $\sigma_{ab,corrected} = (1 + k \cdot ATN)\sigma_{ab,uncorrected}$. $\sigma_{ab,corrected}$ and $\sigma_{ab,uncorrected}$ are the corrected and uncorrected σ_{ab}, respectively. Factor k is set as 0.004 (Zhao et al., 2019b) and ATN is the measured light attenuation by particles collected on the filter of AE51. A recommended compensation of 2.6 for AE51 is introduced here to mitigate the multiple scattering problem (Zhang et al., 2018). Zhao et al. (2019b) added AE33 (3 L/min) to measure the bulk EBC simultaneously while measuring BCPMSD. The bulk EBC from AE33 and the integrated EBC from BCPMSD measured by AE51 were then compared. Results showed that the variation trends and magnitudes of EBC measured by AE33 and AE51 were in good consistence. Therefore, the BCPMSD measured by AE51 was regarded as the measurement results of AE33, and the size-resolved σ_{ab} were retrieved by the constant MAC value of 7.77 m^2/g used in AE33. The traditional BCPMSD is retrieved from AE51-measured size-resolved σ_{ab} with a constant MAC value of 7.77 m^2/g used for AE33. In our new method, the MAC is variable as a function of BC core size (D$_{BC}$) and particle diameter (D$_{particle}$).

For scattering correction, a scattering correction factor C_f is required to account for the scattering effect of the filter matrix: $\sigma_{ab,corrected} = \sigma_{ab,uncorrected}/C_f$. C_f is determined by simultaneous measurement of σ_{ab} by PASS-3 ($\sigma_{ab,PASS-3}$) and AE33 ($\sigma_{ab,AE33}$). $\sigma_{ab,PASS-3}$ is considered as $\sigma_{ab,corrected}$ and $\sigma_{ab,AE33}$ is considered as $\sigma_{ab,uncorrected}$. The wavelengths of PASS-3 and AE33 are not the same. The measured wavelengths of AE33 (370 nm, 470 nm, 520 nm, 590 nm, 660 nm, 880 nm and 950 nm) were interpolated to the measured wavelengths of PASS-3 (405 nm, 532 nm, and 781 nm). Specifically, For AE33, 405 nm, 532 nm and 781 nm are calculated at wavelengths pairs of (370 nm, 470 nm), (520 nm, 590 nm) and (660 nm, 880 nm) through Ångström relationship:

$$\frac{\sigma_{ab}(\lambda_1)}{\sigma_{ab}(\lambda_2)} = \left(\frac{\lambda_1}{\lambda_2}\right)^{-\alpha_{ab}}.$$

More detailed information can be found in Zhao et al. (2020). Measurement results at Taizhou and Beijing showed that all the ratios of σ_{ab} measured by AE33 with a measurement flowrate of 3 L/min and PASS-3 with flowrate of 1 L/min at the three wavelengths varied slightly over the East and North China Plain (± 0.04), with an average value of 2.9. Therefore, as the measurement results between AE33 and AE51 were consistent, all the size-resolved σ_{ab} from AE51 adopted in this study were corrected with $C_f = 2.9$. For the SP2 system, the aerosol samples were analyzed in SP2 (0.12 L/min) to identify the BC-containing particles and in CPC (0.28 L/min) to count the total number of particles. When a BC-containing particle travels through the laser beam (1064 nm) inside the SP2, it emits incandescent light. The avalanche photodetectors (APDs) around the laser beam can detect the incandescence signal. Then the BC-containing particle is detected. N$_{BC}$ can be determined as the ratio of the number of BC-containing particle to that of total aerosol particle. Detailed configuration of the SP2 system has been demonstrated in a previous study (Zhao et al., 2019a). According to the measurements at Taizhou, only 17% of the ambient particles contained BC averagely for bulk aerosol populations. All the measurement systems at the three sites are shown in Fig. S1 in the supplement.

3 Method

131 For current filter-based intruments, EBC are generally derived from σ_{ab} under assumption of a constant MAC value. However, the

132 MAC values are enhanced by different degrees when BC particles are mixed with other weakly-absorbing materials, leading to large

133 uncertainties on EBC retrieval. In order to gain more accurate EBC, it is critical to consider the discrepancies in MAC caused by

134 variations in the coating process, BC sizes, etc. Among with the core-shell configuration hypothesis, developing the relationship

135 between MAC, D_{BC}, and T_{shell} is a new approach to correlate EBC with σ_{ab}.

3.1 Core-shell geometry of aerosol particles

137 To evaluate the theoretical discrepancies in MAC values caused by the corresponding impact factors, a proper model is required to

138 simulate the optical properties of BC-containing particles to a good approximation. Three widely employed mixing states are used

139 to represent the structure of BC-containing aerosols: internal, external, and core-shell model (Ma et al., 2011;China et al., 2015).

140 Generally, freshly-emitted BC particles are chain-like aggregates of small spheres. During the coating process, the chain-like BC

141 aggregates become more compact as they collapse and are coated as a core by organic and inorganic materials (Bond and Bergstrom,

142 2006). Therefore, core-shell configuration is more plausible (Jacobson, 2000). Ma et al. (2012) also indicated that the core-shell

143 assumption can provide a better performance in optical closure than the internal or external models. Furthermore, Moffet et al. (2016)

144 studied particle mixing state and morphology using scanning transmission X-ray microscopy and highlighted that core-shell

145 structure dominated the mixing state of ambient aerosol particles. As aerosols are assumed to be core-shell mixed, with a spherical

146 BC core in the center of the coating sphere. Therefore, the Mie model was used to simulate the optical properties of BC particles

147 with core-shell mixing state. The consistency in observed and theoretical values obtained using Mie and core-shell morphology

148 support the suitability of this method (Cappa et al., 2012).

3.2 Simulation of MAC for BC-containing particle using Mie theory

150 Many optical simulations for BC particles with concentric sphere geometry have been reported and the corresponding results show

151 that the absorption of a pure BC particle will be enhanced when a shell composed of non-absorbing material deposits on this pure

152 BC particle. Since the optical properties were focused on rather than chemical compositions of the mixed aerosols, a simplified

153 hypothesis of BC/sulfate mixtures, which is common in the atmosphere (Khalizov et al., 2009), was introduced in the algorithm for

154 calculating EBC.

155 The reason of AE33 using 880 nm to determine EBC is that aerosol absorption at 880 nm is mainly from BC (Ramachandran and

156 Rajesh, 2007). At shorter wavelength, absorption of organic carbon is not negligible any more, leading to difficulty of extracting

157 BC absorption from total aerosol absorption. Therefore, MAC at 880 nm is discussed in this study and the MAC distribution for a

158 wide range of core and coating sizes at the wavelength of 880 nm are simulated with Mie scattering theory. The refractive index

159 (RI), dependent on light wavelength, is an important parameter to determine aerosol optical properties. However, due to different

160 sources of BC, both the real and imaginary part of RI varies over a significantly wide range. Liu et al. (2018) summarized RI values

161 for specific wavelengths and showed that the real part is generally in the range of 1.5 to 2.0 while the imaginary part usually varies

162 from 0.5 to 1.1 (Sorensen, 2001;Bond and Bergstrom, 2006). Therefore, the real part and imaginary part of RI were set to change

163 from 1.5 to 2.0 and from 0.5 to 1.1, respectively, with a step increase of 0.01. Meanwhile, the RI of sulfate was set as $1.55\text{-}10^{-6}i$ and

164   the density of BC was set as 1.8 g/cm^3, similar to Bond et al. (2006). A total of 3111 values were obtained, and the mean values are

165   illustrated in Fig. 1. The D_{BC} and total aerosol particle diameter ($D_{particle} = D_{BC} + T_{shell}$) ranged from 10 to 700 nm.

166   Figure 1 presents several features of the variation pattern of MAC at 880 nm. MAC values varied significantly with D_{BC} and the

167   thickness of non-absorbing coating, which indicated that light absorption of BC-containing particles was sensitive to the BC core

168   and the coating. When the D_{BC} was less than 100 nm, the thickness of the coating dominated the variation of MAC values, and MAC

169   values increased with increasing T_{shell}. As the T_{shell} increased, the lensing effect became more significant, the light absorption

170   consequently also increased with increasing T_{shell}. MAC value can increase from 4 m^2/g to about 17 m^2/g when the total aerosol size

171   reached up to 700 nm, which indicated that light absorption can be enhanced significantly by the coating. When the D_{BC} was larger

172   than about 100 nm, both T_{shell} and D_{BC} determined MAC values and D_{BC} played a more important role considering that the majority

173   of the contour lines tilted to the axis of particle diameter. MAC increased with increasing T_{shell} and decreased with increasing D_{BC}.

174   At this range ($D_{BC} > 100$ nm), the coating still enhanced absorption. For pure BC particle, MAC decreased with increasing D_{BC}

175   when $D_{BC} > \sim 220$ nm, which indicated that the absorption of large BC particles was less than that of small BC particles per unit

176   mass. If the $D_{particle}$ or the coating (T_{shell}) was fixed, larger D_{BC} generally corresponded to a smaller MAC. Not only did the MAC of

177   coated BC-containing particle vary significantly, but the variation of MAC of pure BC particle was also nonnegligible. For smaller

178   pure BC particle, the MAC increased slightly with BC size until D_{BC} reached 220 nm. Then, MAC decreased with increasing D_{BC}.

179   Therefore, light absorption can be significantly influenced by coating state, and a constant MAC value of 7.77 m^2/g used in AE33

180   is only appropriate for a very limited condition.

181   **3.3 New method to retrieve EBC by considering the variation of MAC**

182   In this subsection, a new method is introduced to determine EBC from the measured σ_{ab}. At a given $D_{particle}$ ($=D_{BC} + T_{shell}$) selected

183   by DMA, if D_{BC} is prescribed, the corresponding T_{shell} is determined. Combining the simultaneously measured particle number

184   concentration ($N(D_{particle})$) by CPC downstream the DMA and the prescribed N_{BC}, the number of BC-containing particles

185   ($N_{BC}(D_{particle})$) is then determined. σ_{ab} can then be calculated by Mie model with $D_{particle}$, D_{BC} and $N_{BC}(D_{particle})$. If the calculated

186   σ_{ab} matches measured σ_{ab} by AE51, then the prescribed D_{BC} is considered as diameter of BC core at $D_{particle}$. Else, D_{BC} is changed

187   until calculated σ_{ab} equals measured σ_{ab}. MAC can be calculated by Mie model with $D_{particle}$, D_{BC} and a presumed BC density.

188   EBC at $D_{particle}$ is then derived by dividing measured σ_{ab} by MAC. BCPMSD can then be derived through changing $D_{particle}$ selected

189   by DMA.

190   As the absorption properties of BC particles in different coating states have been evaluated with the Mie model, as shown in Fig. 1,

191   a simplified algorithm was proposed for deriving BCPMSD through a pre-calculated look-up table. For each $D_{particle}$ selected by

192   DMA, if a D_{BC} is assumed, the corresponding MAC of the particle can be derived from the look-up table. Then, the σ_{ab} can be

193   derived from the MAC, the assumed BC density (1.8 g/cm^3 in this study), and N_{BC} (17% for each $D_{particle}$). We adjusted the guessed

194   D_{BC} until the difference between calculated and measured σ_{ab} was within an acceptable range (0.1%). Consequently, the D_{BC} and

195   thus the EBC at $D_{particle}$ was determined. The EBC at different aerosol sizes were derived separately. Finally, the size-resolved EBC

196   and the bulk EBC were obtained. The iterative procedure is illustrated in Fig. 2.

197 It should be pointed out that the retrieval algorithm of BCPMSD is based on the assumption that BC-containing particles of a fixed

198 diameter are all core-shell mixed and the corresponding D_{BC} for a specific $D_{particle}$ is same. The uncertainties caused by using

199 idealized core-shell model was discussed in section 5.1. A constant number percentage (17%) of BC-containing particles was

200 adopted in this study. However, the BC-containing particle fraction varied with the primary source, time, coagulation, and extent of

201 atmospheric process. The influence attributed to the constant fraction of BC-containing particles was discussed in section 5.2.

202 Additionally, Bond et al. (2013) summarized the density for different graphitic materials. The density values are $1.8 – 2.1$ g/cm^3 for

203 pure graphite, $1.8 – 1.9$ g/cm^3 for pressed pellets of BC, and 1.718 g/cm^3 for fullerene soot. A constant density (1.8 g/cm^3) for BC

204 was briefly used to calculate MAC and BC mass from the volume of particles with a diameter of D_{BC}. Therefore, the uncertainty of

205 derived EBC in this study simply depends on the ratio of 1.8 g/cm^3 and the real density. Finally, the MAC values in the look-up

206 table were the mean values for different RI and the corresponding effects were discussed in section 5.3.

207 **4 Results and discussion**

208 Figure 3 provides a comprehensive overview of the variations in measured and retrieved size-resolved parameters during the

209 campaign. As evident from Fig. 3(a), for the BCPMSD derived by the new method, two modes were found. Figure 4(a) shows the

210 averaged BCPMSD derived from the new method and AE33 during the campaign. The fine mode was located between $97 – 240$

211 nm while the coarse mode was located between $240 – 602$ nm. Figure 3(b) represents the relative deviations between the BCPMSD

212 derived from the newly proposed method and those derived from a constant MAC value of 7.77 m^2/g at 880 nm. The results show

213 that there exist two opposite deviation trends before and after the turning point around 280nm. For aerosol particles larger than 280

214 nm, the EBC derived by the new method were mostly lower than those derived with the constant MAC value of 7.77 m^2/g at 880

215 nm. In contrast, when aerosol particles were smaller than 280 nm, the EBC from the new method were significantly higher than

216 those calculated by the constant MAC, as shown in Fig. 3(c). Figure 3(c) shows the time series of size-resolved MAC during the

217 derivation process of BCPMSD. According to Fig. 3(c), for aerosol particles smaller than 280 nm, the corresponding MAC was

218 almost lower than 7.77 m^2/g at 880 nm. This is because the MAC values of particles smaller than 280 nm are mostly lower than

219 7.77 m^2/g, as represented in Fig. 1. A smaller MAC implies a weaker absorption ability, which means that the same measured σ_{ab}

220 will correspond to an increased EBC. Therefore, more EBC were derived from the new method. For aerosol particles larger than

221 280 nm, in order to match the measured σ_{ab}, the corresponding D_{BC} were generally found to be in those regions of look-up table

222 where the MAC values were larger than 7.77 m^2/g at 880 nm (Fig. 3(c)). Thus, the BC mass loadings for particles larger than 280

223 nm were found to be less than those calculated with the constant MAC value of 7.77 m^2/g at 880 nm. From Fig. 3(c), it can be seen

224 that MAC varied from less than 4 m^2/g to larger than 10 m^2/g at 880 nm, which implies a large variability of the absorption ability

225 of BC-containing particle. Therefore, if the conversion between EBC and σ_{ab} is required, the consideration of variation in mixing

226 state is highly recommended. The simultaneously measured scattering coefficients at 525 nm were introduced here to represent air

227 pollution. As shown in Fig. 3(d), the observation station experienced different levels of pollution. Deviations of EBC derived from

228 the newly proposed method and the constant MAC at different aerosol sizes did not show dependencies on pollution conditions.

229 Figure 3(e) shows the time series of EBC at fine and coarse modes. The EBC were more concentrated in the fine mode than in the

230 coarse mode. The EBC at fine mode were found to be higher than those at the coarse mode for 73% of the campaign duration. The

231 variation trends of bulk EBC calculated by considering the variations of MAC and a constant MAC were similar (Fig. 3(f)). The

232 bulk EBC calculated by the new method were higher than those derived by the constant MAC in 83% of the campaign duration.

233 The EBC calculated from the new method and AE33 for different aerosol size ranges were statistically analyzed. As shown in Fig.

234 4, for all EBC of aerosols ranging between 97 – 602 nm and 97 – 280 nm derived from new method and AE33, strong linear

235 relationships were observed with correlation coefficients of 0.99 and 1.00, respectively. The ratios between the EBC derived from

236 AE33 and the new method for aerosol diameter ranges of 97 – 602 nm and 97 – 280 nm were 0.84 and 0.69, respectively, indicating

237 that the EBC obtained from AE33 was 16% lower for bulk aerosol particles and 31% lower for aerosols smaller than 280 nm. For

238 the diameter range of 280 – 602 nm, MAC values varied significantly and the deviations in EBC derived from the new method and

239 AE33 were divided into two types with a boundary of 0.7 μg/m^3. If the EBC derived from AE33 was lower than 0.7 μg/m^3, there

240 was a relatively consistent ratio of 1.13 between the EBC from the new method and AE33, with a correlation coefficient of 0.95.

241 Therefore, BC mass loading from the AE33 algorithm was 13% higher for aerosol particles larger than 280 nm and EBC lower than

242 0.7 μg/m^3. However, when the EBC derived from AE33 was larger than 0.7 μg/m^3, data points become discrete, and the relationship

243 between the EBC derived from AE33 and the new method could be expressed through an equation (y = 0.29 + 0.48x). However,

244 these comparisons for aerosols at different size ranges were obtained based on the measurements in the NCP. Additionally, the

245 number of samples where EBC of 280 – 602 nm were larger than 0.7 μg/m^3 was too small. Further studies on BCPMSD in

246 conjunction with the PNSD measurements at different sites need to be carried out.

247 **5 Uncertainty analysis**

248 **5.1 The uncertainties of MAC caused by using idealized core-shell model**

249 An idealized concentric core-shell model with a spherical BC core fully coated by sulfate was configured to study the MAC of BC

250 aerosols and derive the EBC in this study. However, freshly emitted BC particles were found to normally exist in the form of loose

251 cluster-like aggregates with numerous spherical primary monomers (Liu et al., 2015). Soon after, these aggregates become coated

252 with other components and collapsed to a more compact form during the coating process (Zhang et al., 2008;Peng et al., 2016).

253 Therefore, the uncertainty in the idealized core-shell configuration is discussed in this subsection.

254 **5.1.1 The formation of BC aggregates with a determined morphology**

255 The fractal aggregates of BC have been well described by fractal geometries through the well-known statistical scaling law

256 (Sorensen, 2001):

257
$$N = k_f \left(\frac{R_g}{a}\right)^{D_f},$$

258 where N is the number of "same-sized" monomers in the cluster, a is the monomer radius, D_f and k_f are known as the fractal

259 dimension and fractal prefactor respectively, determining the morphology of BC cluster. The compactness of a fractal aggregate

260 increses with increasing D_f or k_f. R_g is the gyration radius, infering the overall aggregate radius, determined by

261
$$R_g = \sqrt{\frac{1}{N} \sum_{i=1}^{N} r_i{}^2},$$

262 where r_i represents the distance of the i-th monomer from the center of mass of BC cluster.

263 In order to generate fractal-like aggregates with given N, R_g, a, D_f and k_f, the sequential algorithm proposed in Filippov et al.

264 (2000) is introduced in this study to add the primary monomers one by one. On condition that there is an aggregate including $N-1$

265 monomers, the N-th monomer is constantly placed randomly until it has at least one contact point with the previously attached

266 $N-1$ monomers with no overlapping. Besides, the mass center of the next N-th monomer must obey the rule as follows:

267
$$(r_N - r_{N-1})^2 = \frac{N^2 a^2}{N-1} \left(\frac{N}{k_f}\right)^{2/D_f} - \frac{Na^2}{N-1} - Na^2 \left(\frac{N-1}{k_f}\right)^{2/D_f},$$

268 where r_{N-1} and r_N are the mass center of the first $N-1$ monomers and the N-th monomer, respectively. After the fractual

269 configuration of BC aggregates, the absorption properties of BC containing particles need to be evaluate.

270 The fractal dimensions for aged BC aggregates are generally close to 3 (Kahnert et al., 2012). The aim of this study is to evaluate

271 the effects of aerosol microphysics on the absorption enhancement of fully coated BC particles, which can be regarded as the aged

272 BC aerosols. Therefore, the fractal dimension D_f is set to be 2.8 and k_f is generally set to be 1.2. The diameter of the primary

273 monomers is usually between 20-50 nm and the number of the primary monomers for an aggregates is between 50-300. The size of

274 BC core calcuated by the new method is smaller than 300 nm most of the time during Zhangqiu campaign. The diameter of primary

275 monomers is set to be 50 nm and the number of the primary monomers for an aggregates ranges from 2 to 200, leading to the largest

276 size of volume equivalent BC core close to 300 nm. The real part of BC is generally in the range of 1.5 to 2.0 while the imaginary

277 part usually varies from 0.5 to 1.1 (Liu et al., 2018). Therefore, the mean value 1.75 for BC real part and 0.8 for BC imaginary part

278 are adopted here to calculate MAC values for BC/sulfate mixtures at the wavelength of 880 nm.

279 **5.1.2 Multiple Sphere T-matrix (MSTM) method**

280 As the traditional Mie model is not available for the fractal aggregates, the widely used MSTM method is employed here to quantify

281 the absorption properties of BC clusters (Mackowski and Mishchenko, 1996;Mackowski, 2014). The addition theorem of vector

282 spherical wave functions is used in MSTM method to describe the mutual interactions among the system. The T-matrix of aggregates

283 used to derive particle optical properties can be obtained from these individual monomers. MSTM method can calculate light

284 scattering and absorption properties of the randomly oriented aggregates without numerical averaging over particle orientations if

285 the position, size and refractive index of every spherical element are given. However, the MSTM method is only applicable to

286 evaluate the aggregates of spheres without overlapping and it is carried out with high computational demand.

287 The deviations showed in Fig. 5 are derived by subtracting MAC values calculated by MSTM model by those calculated by Mie

288 model. The results show that most of the MAC values calculated by assuming BC particles in the form of cluster-like aggregates

289 are smaller when the size of BC core is smaller than 150 nm and the overall deviation is within 4 %, which indicates that Mie theory

290 is a good approximation to the BC aggregates even when D_{BC} reaches 200 nm. When BC core is larger than 200 nm, the MAC

291 values calculated by MSTM model increase with the thickness of shell and will be larger than those derived from concentric core-

292 shell model. The deviations between MAC calculated by the idealized concentric core-shell model and letting BC particles be in the

293 form of cluster-like aggregates are overall within 15%.

294 **5.2 The uncertainties of derived EBC caused by using a constant BC-containing particle fraction**

295 Figure 6 shows the deviation of BCPMSD calculated from different N_{BC} (8.5%, 17%, 34%). For the newly proposed method, using

296 a constant N_{BC} does not change the size-resolved distribution mode. There is still a fine mode and coarse mode with a boundary of

297 240 nm. Besides, the influence of using different N_{BC} to derived EBC is very limited when particles are larger than 200 nm. However,

298 the deviations between the EBC derived from different N_{BC} are large when particles diameters are smaller than 200 nm. At this

299 range, if N_{BC} is underestimated, the EBC will be underestimated. On the contrary, the EBC is overeatimated if N_{BC} is overestimated.

300 **5.3 The uncertainties of MAC caused by variation of RI**

301 As the RI of BC is still reported to vary over a wide range and the MAC used in this study was a mean value, it is critical to assess

302 the impact caused by variation in the real and imaginary parts of RI on the calculated MAC and the derived EBC. For aerosol

303 particles with given D_{BC} and T_{shell}, we calculated the MAC of BC with the real part of RI ranging from 1.5 to 2.0 and imaginary part

304 ranging from 0.5 to 1.1. The step increase of both real and imaginary parts was 0.01 and there were 3111 MAC values for every

305 aerosol particle with given D_{BC} and T_{shell}. The ratio of the standard deviation to the mean value for these 3111 MAC values have

306 been presented to demonstrate the uncertainty in MAC due to the uncertainty of BC RI.

307 Figure 7(a) shows the uncertainties in MAC along different values of D_{BC} and T_{shell}. It shows that aerosol particles with small BC

308 core have larger uncertainties and all the uncertainties were below 24%, implying a large variation in absorption for BC-containing

309 particles with small BC core. When $D_{particle}$ was fixed, the uncertainties decreased with increasing D_{BC}. When D_{BC} was determined,

310 the uncertainties did not change much with T_{shell}, indicating the importance to quantify D_{BC} for BC-containing particles in order to

311 reduce RI-related uncertainty in absorption. For pure BC particles, the uncertainties also decreased with increasing BC particle size

312 significantly from over 22% at 100 nm to less than 2% at 600 nm. Figure 7(b) shows the uncertainties when the imaginary part was

313 fixed at 0.8 and the real part ranged from 1.5 to 2.0 with an interval of 0.01. It can be seen that when the imaginary part of RI was

314 fixed, variations in the real part led to slight uncertainties. All the uncertainties were found to be below 14%. Figure 7(c)

315 demonstrates the uncertainties when the real part was fixed at 1.75 and the imaginary part ranged from 0.5 to 1.1 with an interval

316 of 0.01. Comparing Fig. 7(a) and 7(c), we can see that the patterns of MAC uncertainties were similar. Overall, the uncertainties

317 were dominated by the variations of the imaginary part and only slightly affected by variations in the real part. Therefore, it is highly

318 recommended to reduce the uncertainties in the imaginary part for a more precise absorption measurement.

319 The variation of EBC caused by the uncertainties in RI were further evaluated. As stated in section 3.2, for a MAC (880 nm) point

320 at ($D_{particle}$, D_{BC}) of Fig. 1, it is a mean value averaged with respect to both real part of RI varied from 1.5 to 2.0 and imaginary part

321 of RI varied from 0.5 to 1.1. The mean MAC (880 nm) plus corresponding standard deviation (MAC + Std) and minus corresponding

322 standard deviation (MAC – Std) were used to show the uncertainties in EBC caused by variation of BC RI. As we can see from Fig.

323 8(a), irrespective of the MAC was MAC + Std or MAC – Std, there was no change in the mode of BCPMSD. The derived EBC of

324 all particles ranging from 97 – 602 nm increased when MAC – Std was used and decreased when MAC + Std was used. Compared

325 to the bulk EBC derived by mean MAC, those derived by MAC – Std were higher within 35% (Fig. 8(b)). The decrease in the

326 derived EBC caused by MAC + Std was less than the increase in the derived EBC caused by the MAC – Std. For both fine and

327 coarse mode particles, the deviations in EBC caused by MAC + Std or MAC – Std were also within 35% (Fig. 8(c) and Fig. 8(d)).

328 This sensitivity study indicates that the accuracy of the derived BCPMSD is sensitive to the accuracy of MAC, especially when the

329 actual MAC is less than the mean MAC.

330 **6 Conclusions**

331 There was a significant variability in the MAC values of BC with the size of BC core and the thickness of coating, which exerted a

332 significant influence on the optical method for deriving EBC. In this study, a new method was proposed to derive EBC considering

333 the lensing effect of core-shell structure and the consequent MAC variations in MAC.

334 A look-up table describing the variations of MAC at 880 nm attributed to the coating state and size of BC core was established

335 theoretically using Mie simulation and assuming a core-shell configuration for BC-containing aerosols. The MAC at 880 nm varied

336 significantly with different sizes of core and shell from less than 2 m^2/g to over 16 m^2/g, indicating a large variation in absorption

337 ability for BC-containing particle. Then, the EBC at different aerosol sizes were derived by finding an appropriate BC core

338 configured with a MAC value from the look-up table to close the calculated and measured σ_{ab}.

339 This newly proposed method was applied to a campaign measurement in the NCP. There were two modes for BCPMSD at the

340 accumulation mode separated by 240 nm. For 73% of the cases, the EBC of the fine mode were larger than those of the coarse mode

341 during the measurement. The EBC derived by the new method were mostly lower than those derived by a constant MAC of 7.77

342 m^2/g for particles larger than 280 nm, and higher for particles smaller than 280 nm. Similarly, the bulk EBC accumulated from

343 BCPMSD derived from the new method were mostly higher than those derived from a constant MAC of 7.77 m^2/g.

344 Uncertainty analysis was carried out with respect to assumptions used in this study. The uncertainty caused by idealized core-shell

345 model was analyzed by substituting the core with cluster-like aggregates using MSTM method, and the resulting relative

346 uncertainties were within 15%. The uncertainties caused by using a constant number fraction of BC-containing particle was analyzed

347 by halving and doubling its value, and the results showed that particle larger than 200 nm was insensitive to the number fraction of

348 BC-containing particle, whereas, for particle smaller than 200 nm, the EBC would be underestimated if the BC-containing particle

349 fraction was underestimated. The uncertainty in derived EBC that was caused due to the wide range of RI of the BC core was also

350 studied. The results indicated that the uncertainty of the imaginary part results in larger uncertainties to the MAC compared with

351 the real part. The relative uncertainty of the derived EBC was within 35%.

352 This study provides a new way to derive EBC from σ_{ab} for the widely-used filter-based measurements. This research deepens our

353 understanding of the uncertainty in measured EBC caused by the utilization of a constant MAC and illustrates the great necessity to

354 take the variation of MAC into account. The new method improves the measurements of BCPMSD and deepens the understanding

355 about the significant influence of mixing state on the absorption of BC.

356 **Data availability**

357 The measurement data involved in this study are available upon request to the authors.

References

Bond, T. C., and Bergstrom, R. W.: Light absorption by carbonaceous particles: An investigative review, Aerosol Science and Technology, 40, 27-67, 10.1080/02786820500421521, 2006.

Bond, T. C., Habib, G., and Bergstrom, R. W.: Limitations in the enhancement of visible light absorption due to mixing state, J. Geophys. Res.-Atmos., 111, 13, 10.1029/2006jd007315, 2006.

Bond, T. C., Doherty, S. J., Fahey, D. W., Forster, P. M., Berntsen, T., DeAngelo, B. J., Flanner, M. G., Ghan, S., Karcher, B., Koch, D., Kinne, S., Kondo, Y., Quinn, P. K., Sarofim, M. C., Schultz, M. G., Schulz, M., Venkataraman, C., Zhang, H., Zhang, S., Bellouin, N., Guttikunda, S. K., Hopke, P. K., Jacobson, M. Z., Kaiser, J. W., Klimont, Z., Lohmann, U., Schwarz, J. P., Shindell, D., Storelvmo, T., Warren, S. G., and Zender, C. S.: Bounding the role of black carbon in the climate system: A scientific assessment, J. Geophys. Res.-Atmos., 118, 5380-5552, 10.1002/jgrd.50171, 2013.

Cappa, C. D., Onasch, T. B., Massoli, P., Worsnop, D. R., Bates, T. S., Cross, E. S., Davidovits, P., Hakala, J., Hayden, K. L., Jobson, B. T., Kolesar, K. R., Lack, D. A., Lerner, B. M., Li, S. M., Mellon, D., Nuaaman, I., Olfert, J. S., Petaja, T., Quinn, P. K., Song, C., Subramanian, R., Williams, E. J., and Zaveri, R. A.: Radiative Absorption Enhancements Due to the Mixing State of Atmospheric Black Carbon, Science, 337, 1078-1081, 10.1126/science.1223447, 2012.

Cappa, C. D., Zhang, X. L., Russell, L. M., Collier, S., Lee, A. K. Y., Chen, C. L., Betha, R., Chen, S. J., Liu, J., Price, D. J., Sanchez, K. J., McMeeking, G. R., Williams, L. R., Onasch, T. B., Worsnop, D. R., Abbatt, J., and Zhang, Q.: Light absorption by ambient black and brown carbon and its dependence on black carbon coating state for two California, USA, cities in winter and summer, J. Geophys. Res.-Atmos., 124, 1550-1577, 10.1029/2018jd029501, 2019.

Castagna, J., Calvello, M., Esposito, F., and Pavese, G.: Analysis of equivalent black carbon multi-year data at an oil pre-treatment plant: Integration with satellite data to identify black carbon transboundary sources, Remote Sens. Environ., 235, 10, 10.1016/j.rse.2019.111429, 2019.

China, S., Scarnato, B., Owen, R. C., Zhang, B., Ampadu, M. T., Kumar, S., Dzepina, K., Dziobak, M. P., Fialho, P., Perlinger, J. A., Hueber, J., Helmig, D., Mazzoleni, L. R., and Mazzoleni, C.: Morphology and mixing state of aged soot particles at a remote marine free troposphere site: Implications for optical properties, Geophys. Res. Lett., 42, 1243-1250, 10.1002/2014gl062404, 2015.

Filippov, A. V., Zurita, M., and Rosner, D. E.: Fractal-like aggregates: Relation between morphology and physical properties, J. Colloid Interface Sci., 229, 261-273, 10.1006/jcis.2000.7027, 2000.

Fuller, K. A., Malm, W. C., and Kreidenweis, S. M.: Effects of mixing on extinction by carbonaceous particles, J. Geophys. Res.-Atmos., 104, 15941-15954, 10.1029/1998jd100069, 1999.

Hansen, A. D. A., Rosen, H., and Novakov, T.: The aethalometer - an instrument for the real-time measurement of optical-absorption by aerosol-particles, Sci. Total Environ., 36, 191-196, 10.1016/0048-9697(84)90265-1, 1984.

Helin, A., Niemi, J. V., Virkkula, A., Pirjola, L., Teinila, K., Backman, J., Aurela, M., Saarikoski, S., Ronkko, T., Asmi, E., and Timonen, H.: Characteristics and source apportionment of black carbon in the Helsinki metropolitan area, Finland, Atmospheric Environment, 190, 87-98, 10.1016/j.atmosenv.2018.07.022, 2018.

Highwood, E. J., and Kinnersley, R. P.: When smoke gets in our eyes: The multiple impacts of atmospheric black carbon on climate, air quality and health, Environment International, 32, 560-566, 10.1016/j.envint.2005.12.003, 2006.

Jacobson, M. Z.: A physically-based treatment of elemental carbon optics: Implications for global direct forcing of aerosols, Geophys. Res. Lett., 27, 217-220, 10.1029/1999gl010968, 2000.

Kahnert, M., Nousiainen, T., Lindqvist, H., and Ebert, M.: Optical properties of light absorbing carbon aggregates mixed with sulfate: assessment of different model geometries for climate forcing calculations, Optics Express, 20, 17, 10.1364/oe.20.010042, 2012.

Khalizov, A. F., Xue, H. X., Wang, L., Zheng, J., and Zhang, R. Y.: Enhanced light absorption and scattering by carbon soot aerosol internally mixed with sulfuric acid, Journal of Physical Chemistry A, 113, 1066-1074, 10.1021/jp807531n, 2009.

Lack, D. A., and Cappa, C. D.: Impact of brown and clear carbon on light absorption enhancement, single scatter albedo and absorption wavelength dependence of black carbon, Atmospheric Chemistry and Physics, 10, 4207-4220, 10.5194/acp-10-4207-2010, 2010.

Lack, D. A., Langridge, J. M., Bahreini, R., Cappa, C. D., Middlebrook, A. M., and Schwarz, J. P.: Brown carbon and internal mixing in biomass burning particles, Proceedings of the National Academy of Sciences of the United States of America, 109, 14802-14807, 10.1073/pnas.1206575109, 2012.

Li, Z. J., Tan, H. B., Zheng, J., Liu, L., Qin, Y. M., Wang, N., Li, F., Li, Y. J., Cai, M. F., Ma, Y., and Chan, C. K.: Light absorption properties and potential sources of particulate brown carbon in the Pearl River Delta region of China, Atmospheric Chemistry and Physics, 19, 11669-11685, 10.5194/acp-19-11669-2019, 2019.

Liu, C., Yin, Y., Hu, F. C., Jin, H. C., and Sorensen, C. M.: The effects of monomer size distribution on the radiative properties of black carbon aggregates, Aerosol Science and Technology, 49, 928-940, 10.1080/02786826.2015.1085953, 2015.

Liu, C., Chung, C. E., Yin, Y., and Schnaiter, M.: The absorption Angstrom exponent of black carbon: from numerical aspects, Atmospheric Chemistry and Physics, 18, 6259-6273, 10.5194/acp-18-6259-2018, 2018.

Liu, H., Pan, X. L., Wu, Y., Wang, D. W., Tian, Y., Liu, X. Y., Lei, L., Sun, Y. L., Fu, P. Q., and Wang, Z. F.: Effective densities of soot particles and their relationships with the mixing state at an urban site in the Beijing megacity in the winter of 2018, Atmospheric Chemistry and Physics, 19, 14791-14804, 10.5194/acp-19-14791-2019, 2019.

Ma, N., Zhao, C. S., Nowak, A., Muller, T., Pfeifer, S., Cheng, Y. F., Deng, Z. Z., Liu, P. F., Xu, W. Y., Ran, L., Yan, P., Gobel, T., Hallbauer, E., Mildenberger, K., Henning, S., Yu, J., Chen, L. L., Zhou, X. J., Stratmann, F., and Wiedensohler, A.: Aerosol optical properties in the North China Plain during HaChi campaign: an in-situ optical closure study, Atmospheric Chemistry and Physics, 11, 5959-5973, 10.5194/acp-11-5959-2011, 2011.

Ma, N., Zhao, C. S., Muller, T., Cheng, Y. F., Liu, P. F., Deng, Z. Z., Xu, W. Y., Ran, L., Nekat, B., van Pinxteren, D., Gnauk, T., Mueller, K., Herrmann, H., Yan, P., Zhou, X. J., and Wiedensohler, A.: A new method to determine the mixing state of light absorbing carbonaceous using the measured aerosol optical properties and number size distributions, Atmospheric Chemistry and Physics, 12, 2381-2397, 10.5194/acp-12-2381-2012, 2012.

Mackowski, D. W., and Mishchenko, M. I.: Calculation of the T matrix and the scattering matrix for ensembles of spheres, J. Opt. Soc. Am. A-Opt. Image Sci. Vis., 13, 2266-2278, 10.1364/josaa.13.002266, 1996.

Mackowski, D. W.: A general superposition solution for electromagnetic scattering by multiple spherical domains of optically active media, Journal of Quantitative Spectroscopy & Radiative Transfer, 133, 264-270, 10.1016/j.jqsrt.2013.08.012, 2014.

Majdi, M., Kim, Y., Turquety, S., and Sartelet, K.: Impact of mixing state on aerosol optical properties during severe wildfires over the Euro-Mediterranean region, Atmospheric Environment, 220, 11, 10.1016/j.atmosenv.2019.117042, 2020.

Moffet, R. C., O'Brien, R. E., Alpert, P. A., Kelly, S. T., Pham, D. Q., Gilles, M. K., Knopf, D. A., and Laskin, A.: Morphology and mixing of black carbon particles collected in central California during the CARES field study, Atmospheric Chemistry and Physics, 16, 14515-14525, 10.5194/acp-16-14515-2016, 2016.

Moosmuller, H., Chakrabarty, R. K., and Arnott, W. P.: Aerosol light absorption and its measurement: A review, Journal of Quantitative Spectroscopy & Radiative Transfer, 110, 844-878, 10.1016/j.jqsrt.2009.02.035, 2009.

Ning, Z., Chan, K. L., Wong, K. C., Westerdahl, D., Mocnik, G., Zhou, J. H., and Cheung, C. S.: Black carbon mass size distributions of diesel exhaust and urban aerosols measured using differential mobility analyzer in tandem with Aethalometer, Atmospheric Environment, 80, 31-40, 10.1016/j.atmosenv.2013.07.037, 2013.

Onasch, T. B., Trimborn, A., Fortner, E. C., Jayne, J. T., Kok, G. L., Williams, L. R., Davidovits, P., and Worsnop, D. R.: Soot Particle Aerosol Mass Spectrometer: Development, Validation, and Initial Application, Aerosol Science and Technology, 46, 804-817, 10.1080/02786826.2012.663948, 2012.

Peng, J. F., Hu, M., Guo, S., Du, Z. F., Zheng, J., Shang, D. J., Zamora, M. L., Zeng, L. M., Shao, M., Wu, Y. S., Zheng, J., Wang, Y., Glen, C. R., Collins, D. R., Molina, M. J., and Zhang, R. Y.: Markedly enhanced absorption and direct radiative forcing of black carbon under polluted urban environments, Proceedings of the National Academy of Sciences of the United States of America, 113, 4266-4271, 10.1073/pnas.1602310113, 2016.

Petzold, A., Ogren, J. A., Fiebig, M., Laj, P., Li, S. M., Baltensperger, U., Holzer-Popp, T., Kinne, S., Pappalardo, G., Sugimoto, N., Wehrli, C., Wiedensohler, A., and Zhang, X. Y.: Recommendations for reporting "black carbon" measurements, Atmospheric Chemistry and Physics, 13, 8365-8379, 10.5194/acp-13-8365-2013, 2013.

Ramachandran, S., and Rajesh, T. A.: Black carbon aerosol mass concentrations over Ahmedabad, an urban location in western India: Comparison with urban sites in Asia, Europe, Canada, and the United States, J. Geophys. Res.-Atmos., 112, 19, 10.1029/2006jd007488, 2007.

Ramanathan, V., and Carmichael, G.: Global and regional climate changes due to black carbon, Nature Geoscience, 1, 221-227, 10.1038/ngeo156, 2008.

Ran, L., Deng, Z. Z., Wang, P. C., and Xia, X. A.: Black carbon and wavelength-dependent aerosol absorption in the North China Plain based on two-year aethalometer measurements, Atmospheric Environment, 142, 132-144, 10.1016/j.atmosenv.2016.07.014, 2016a.

Ran, L., Deng, Z. Z., Xu, X. B., Yan, P., Lin, W. L., Wang, Y., Tian, P., Wang, P. C., Pan, W. L., and Lu, D. R.: Vertical profiles of black carbon measured by a micro-aethalometer in summer in the North China Plain, Atmospheric Chemistry and Physics, 16, 10441-10454, 10.5194/acp-16-10441-2016, 2016b.

Sandradewi, J., Prevot, A. S. H., Szidat, S., Perron, N., Alfarra, M. R., Lanz, V. A., Weingartner, E., and Baltensperger, U.: Using aerosol light absorption measurements for the quantitative determination of wood burning and traffic emission contributions to particulate matter, Environmental Science & Technology, 42, 3316-3323, 10.1021/es702253m, 2008.

Schwarz, J. P., Gao, R. S., Fahey, D. W., Thomson, D. S., Watts, L. A., Wilson, J. C., Reeves, J. M., Darbeheshti, M., Baumgardner, D. G., Kok, G. L., Chung, S. H., Schulz, M., Hendricks, J., Lauer, A., Karcher, B., Slowik, J. G., Rosenlof, K. H., Thompson, T. L., Langford, A. O., Loewenstein, M., and Aikin, K. C.: Single-particle measurements of midlatitude black carbon and light-scattering aerosols from the boundary layer to the lower stratosphere, J. Geophys. Res.-Atmos., 111, 15, 10.1029/2006jd007076, 2006.

Schwarz, J. P., Spackman, J. R., Fahey, D. W., Gao, R. S., Lohmann, U., Stier, P., Watts, L. A., Thomson, D. S., Lack, D. A., Pfister, L., Mahoney, M. J., Baumgardner, D., Wilson, J. C., and Reeves, J. M.: Coatings and their enhancement of black carbon light absorption in the tropical atmosphere, J. Geophys. Res.-Atmos., 113, 10, 10.1029/2007jd009042, 2008.

Sharma, S., Brook, J. R., Cachier, H., Chow, J., Gaudenzi, A., and Lu, G.: Light absorption and thermal measurements of black carbon in different regions of Canada, J. Geophys. Res.-Atmos., 107, 11, 10.1029/2002jd002496, 2002.

Shiraiwa, M., Kondo, Y., Moteki, N., Takegawa, N., Miyazaki, Y., and Blake, D. R.: Evolution of mixing state of black carbon in polluted air from Tokyo, Geophys. Res. Lett., 34, 5, 10.1029/2007gl029819, 2007.

Sorensen, C. M.: Light scattering by fractal aggregates: A review, Aerosol Science and Technology, 35, 648-687, 10.1080/027868201316900007, 2001.

Wu, C., Ng, W. M., Huang, J. X., Wu, D., and Yu, J. Z.: Determination of Elemental and Organic Carbon in PM2.5 in the Pearl River Delta Region: Inter-Instrument (Sunset vs. DRI Model 2001 Thermal/Optical Carbon Analyzer) and Inter-Protocol Comparisons (IMPROVE vs. ACE-Asia Protocol), Aerosol Science and Technology, 46, 610-621, 10.1080/02786826.2011.649313, 2012.

Zhang, R. Y., Khalizov, A. F., Pagels, J., Zhang, D., Xue, H. X., and McMurry, P. H.: Variability in morphology, hygroscopicity, and optical properties of soot aerosols during atmospheric processing, Proceedings of the National Academy of Sciences of the United States of America, 105, 10291-10296, 10.1073/pnas.0804860105, 2008.

Zhang, Y. X., Zhang, Q., Cheng, Y. F., Su, H., Li, H. Y., Li, M., Zhang, X., Ding, A. J., and He, K. B.: Amplification of light absorption of black carbon associated with air pollution, Atmospheric Chemistry and Physics, 18, 9879-9896, 10.5194/acp-18-9879-2018, 2018.

Zhao, G., Tan, T. Y., Zhao, W. L., Guo, S., Tian, P., and Zhao, C. S.: A new parameterization scheme for the real part of the ambient

490   urban aerosol refractive index, Atmospheric Chemistry and Physics, 19, 12875-12885, 10.5194/acp-19-12875-2019, 2019a.

491   Zhao, G., Tao, J. C., Kuang, Y., Shen, C. Y., Yu, Y. L., and Zhao, C. S.: Role of black carbon mass size distribution in the direct

492   aerosol radiative forcing, Atmospheric Chemistry and Physics, 19, 13175-13188, 10.5194/acp-19-13175-2019, 2019b.

493   Zhao, G., Yu, Y., Tian, P., Li, J., Guo, S., and Zhao, C.: Evaluation and Correction of the Ambient Particle Spectral Light Absorption

494   Measured Using a Filter-based Aethalometer, Aerosol and Air Quality Research, 20, 1833-1841, 10.4209/aaqr.2019.10.0500, 2020.

495
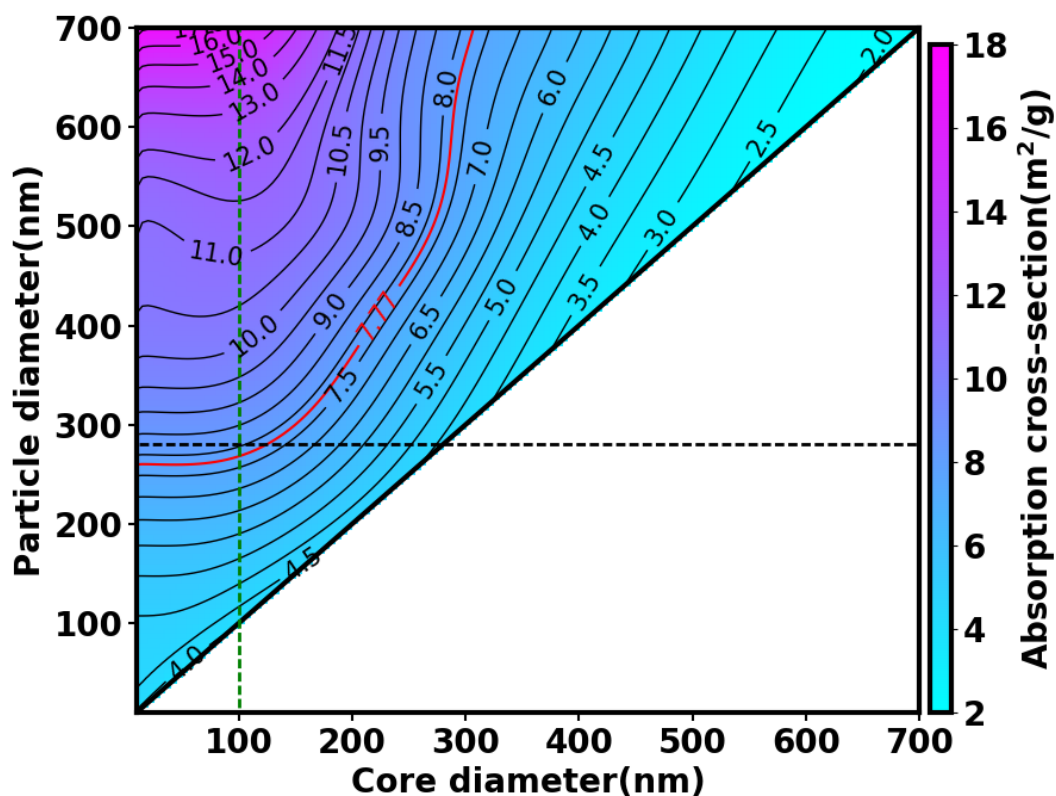
Figure 1. Variations in MAC as a function of D_{BC} and $D_{particle}$, calculated by the concentric core-shell Mie model at the wavelength of 880 nm. The red solid line is the constant MAC value used in AE33. The bold black solid line is the 1:1 line that presents the variations in MAC for pure BC particles with different D_{BC}. The horizontal black dashed line distinguishes particles with a diameter of 280 nm while the vertical green dashed line indicates a D_{BC} of 100 nm.

502
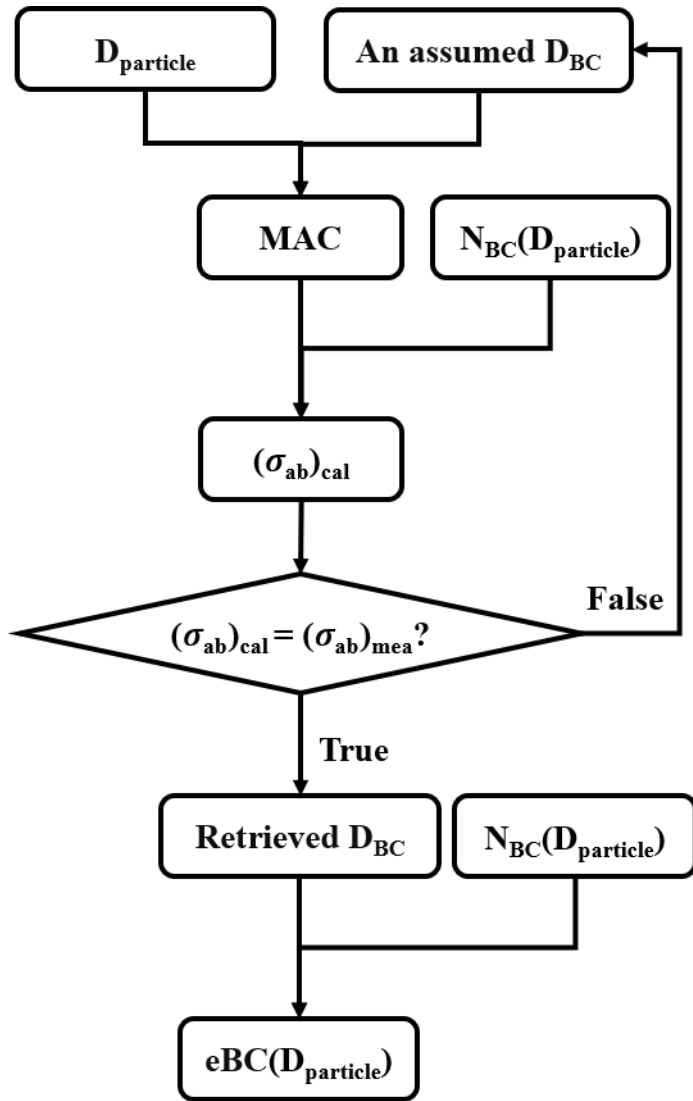
Figure 2. Schematic diagram of the iterative algorithm for retrieving the EBC at a fixed particle diameter based on the look-up table of MAC, particle size and core size. $(\sigma_{ab})_{cal}$ and $(\sigma_{ab})_{mea}$ represent calculated and measured absorption coefficients, respectively. $N_{BC}(D_{particle})$ indicates the number concentration of particle containing BC at the given $D_{particle}$.
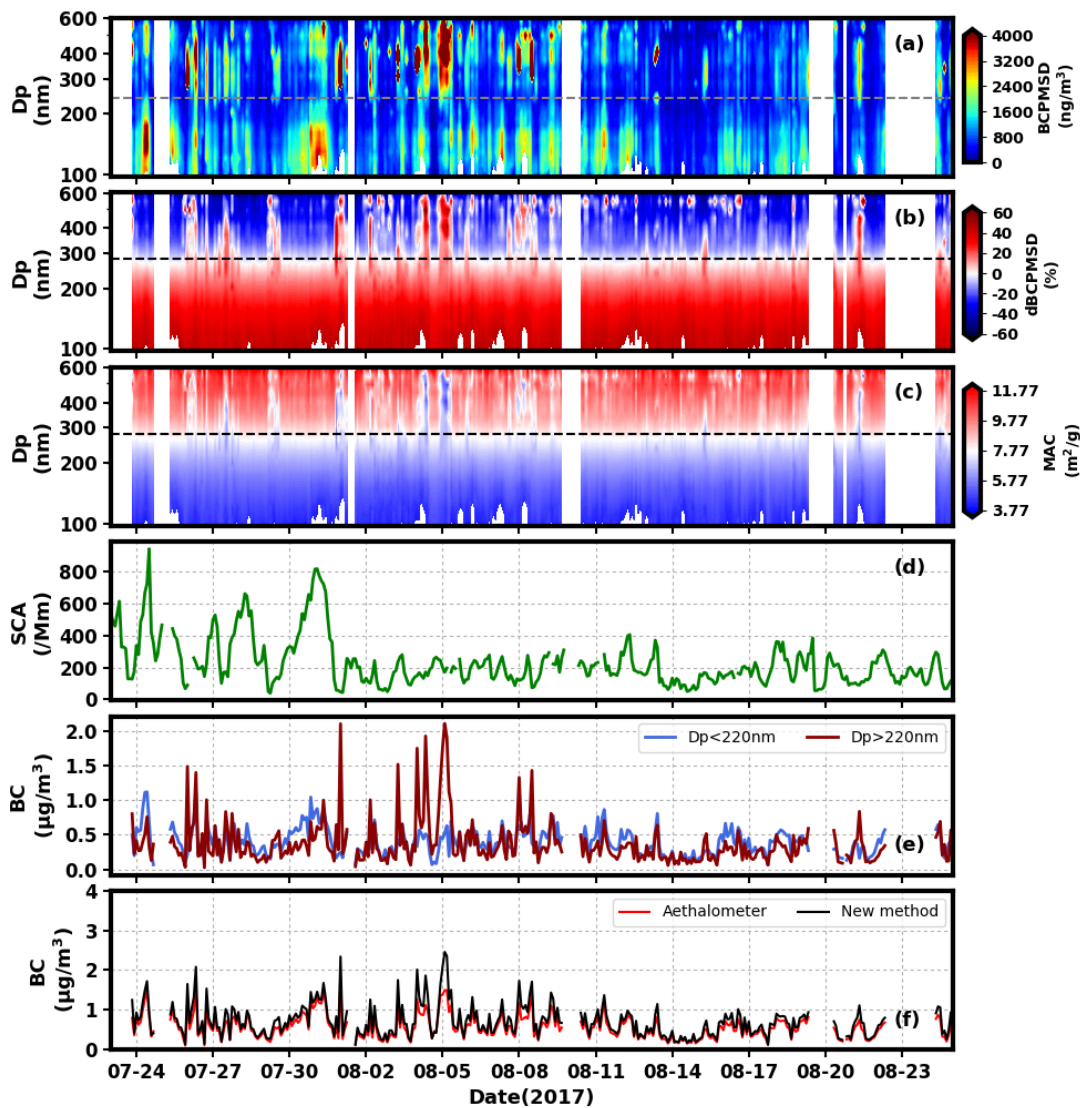
503

504

505

506

507

Figure 3. Time series of (a) the BCPMSD derived from the new method proposed in this work. The dashed line indicates the

particle size of 240 nm; (b) relative deviations between BCPMSD derived from the new method (varied MAC) and constant

MAC at 7.77 m²/g. The dashed line indicates the particle size of 280 nm; (c) the size-resolved MAC. The dashed line indicates

the particle size of 280 nm; (d) the scattering coefficients at 525 nm; (e) the EBC integrated for particles smaller than 220

nm (blue) and larger than 220 nm (red); and (f) the EBC determined by the new method (black) and constant MAC of 7.77

m²/g (red).
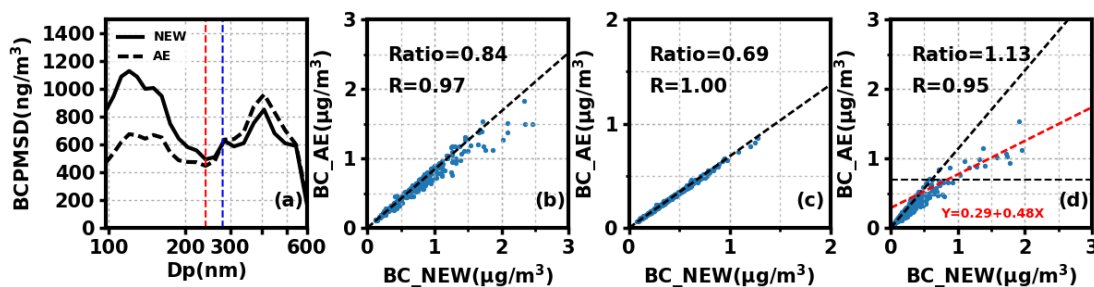
Figure 4. Comparison between the EBC derived from the new method and from constant MAC of 7.77 m²/g used by AE33.

(a) shows the results of the BCPMSD, the dashed black line is the result of constant MAC of 7.77 m²/g used by AE33, and

the solid black line represents the results from the new method; the dashed red line is the split line of 240 nm between fine

mode and coarse mode, and the dashed blue line is the split line of 280 nm between the opposite tendencies of deviations in BCPMSD; (b) the bulk EBC integrated from 97 nm to 602 nm; (c) the fine mode EBC integrated from 97 nm to 280 nm; (d) the coarse mode EBC integrated from 280 to 606 nm; the dashed black line represents boundary of 0.7 μg/m³ and the red dashed line is the regression line for the EBC larger than 0.7 μg/m³.
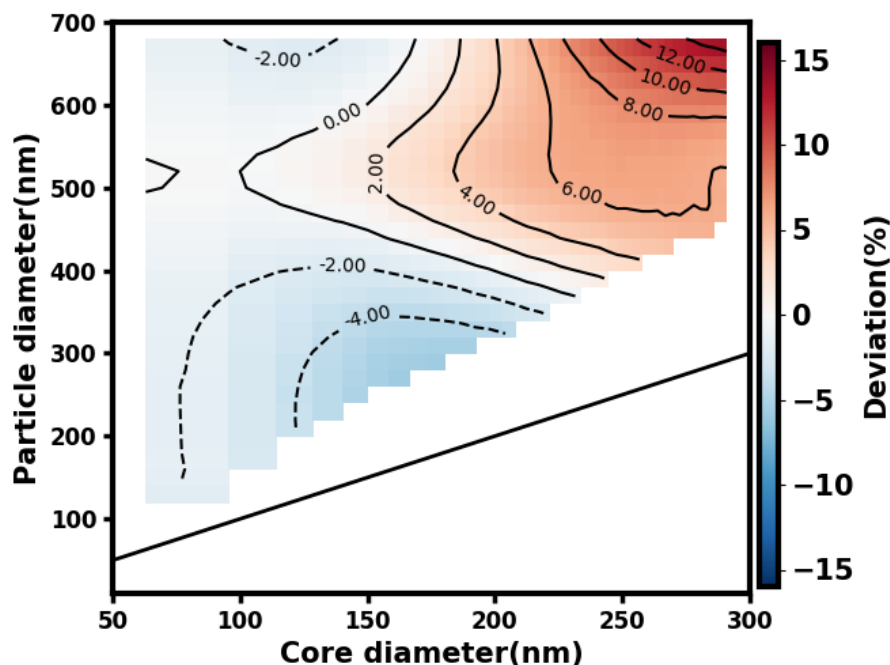
Figure 5. Relative deviations of MAC values calculated by idealized concentric core-shell model and letting BC particles be in the form of cluster-like aggregates. The solid line is 1:1 line.
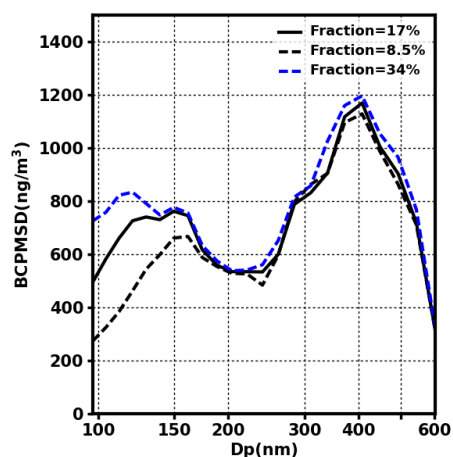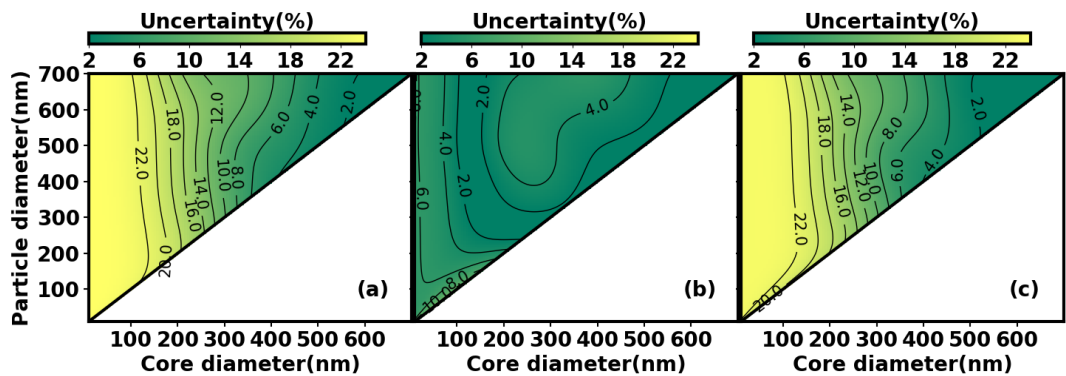

Figure 6. The derived BCPMSD by using different constant BC-containing particle fraction. The solid black line represents the result derived from a fraction of 17%. The dashed black line and blue line show the results derived from a fraction of half of 8.5% and double of 34%.

Figure 7. Uncertainty in MAC of BC when (a) real part of RI ranges from 1.5 to 2.0 and imaginary part ranges from 0.5 to 1.1; (b) real part of RI ranges from 1.5 to 2.0 and imaginary part is fixed at 0.8 and (c) real part of RI is fixed at 1.75 and imaginary part ranges from 0.5 to 1.1. The bold black solid line is the 1:1 line and presents the uncertainty of MAC for pure BC particles with different RI.
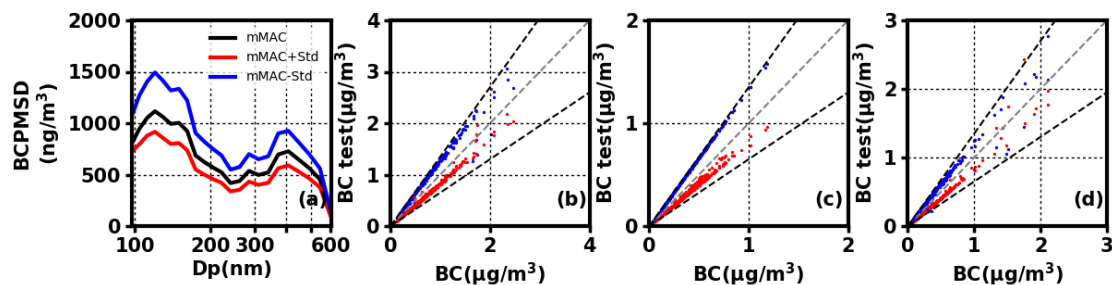
Figure 8. (a) The BCPMSD calculated by using the look up table with mean MAC (black line), mean MAC plus the corresponding standard deviation (red line) and mean MAC minus the corresponding standard deviation (blue line); the EBC derived by the look up table with mean MAC versus those derived by the look up table with mean MAC plus standard deviation (red dots) or mean MAC minus standard deviation (blue dots) for (b) aerosol particles ranging from 97–602 nm; (c) aerosol particles ranging from 97–240 nm (fine mode); and (d) aerosol particles ranging from 240–602 nm (coarse mode). The dashed black line represents the 35% deviation from the 1:1 line (dashed grey lines).